



A LETTERS JOURNAL EXPLORING
THE FRONTIERS OF PHYSICS

OFFPRINT

**Anderson localization of shear waves observed
by magnetic resonance imaging**

S. PAPAZOGLU, D. KLATT, J. BRAUN and I. SACK

EPL, 91 (2010) 17007

Please visit the new website
www.epljournal.org

Anderson localization of shear waves observed by magnetic resonance imaging

S. PAPAZOGLOU^{1(a)}, D. KLATT¹, J. BRAUN² and I. SACK¹

¹ Department of Radiology, Charité University Medicine - Charitéplatz 1, 10117 Berlin, Germany, EU

² Institute of Medical Informatics, Charité University Medicine - Hindenburgdamm 30, 12203 Berlin, Germany, EU

received 26 March 2010; accepted in final form 2 July 2010

published online 30 July 2010

PACS 71.23.An – Theories and models; localized states

PACS 63.20.Pw – Localized modes

PACS 46.40.Cd – Mechanical wave propagation (including diffraction, scattering, and dispersion)

Abstract – In this letter we present for the first time an experimental investigation of shear wave localization using motion-sensitive magnetic resonance imaging (MRI). Shear wave localization was studied in gel phantoms containing arrays of randomly positioned parallel glass rods. The phantoms were exposed to continuous harmonic vibrations in a frequency range from 25 to 175 Hz, yielding wavelengths on the order of the elastic mean free path, *i.e.* the Ioffe-Regel criterion of Anderson localization was satisfied. The experimental setup was further chosen such that purely shear horizontal waves were induced to avoid effects due to mode conversion and pressure waves. Analysis of the distribution of shear wave intensity in experiments and simulations revealed a significant deviation from Rayleigh statistics indicating that shear wave energy is localized. This observation is further supported by experiments on weakly scattering samples exhibiting Rayleigh statistics and an analysis of the multifractality of wave functions. Our results suggest that motion-sensitive MRI is a promising tool for studying Anderson localization of time-harmonic shear waves, which are increasingly used in dynamic elastography.

Copyright © EPLA, 2010

Multiple scattering of waves has been for long a subject of fundamental interest in physical research [1]. It provides an elegant explanation for a multiplicity of effects in ordered and disordered media such as band structure, random lasing [2], coherent backscattering [3], and disorder-driven metal-insulator transitions [4]. Originally introduced as a possible mechanism for metal-insulator transitions, Anderson localization has also attracted a lot of attention in classical wave propagation [5]. In Anderson localization, constructive interference of multiply scattered waves leads to the confinement of most of the wave intensity in finite regions inside a disordered medium. Outside these regions the intensity decreases exponentially on a scale given by the localization length. Classical waves offer the possibility to study this effect without the ubiquitous Coulomb interaction in electronic systems, which is known to show similar effects [6]. In the past few decades Anderson localization of classical waves was studied experimentally in two and three spatial dimensions for electromagnetic and acoustic waves [7–14]. However, absorption and the necessity to use strongly

scattering samples have often complicated the observation of Anderson localization of classical waves [7,9,10]. So far most investigations on elastic waves have focused on sound waves while the localization of shear waves has not yet been addressed experimentally. Since shear waves are increasingly important for probing the mechanical connectivity and rigidity of soft biological tissues we are interested to study Anderson localization in tissue-mimicking gels using motion-sensitive magnetic resonance imaging (MRI).

The motion sensitivity of MRI originates in the phase of the complex MR signal which scales with the large gyromagnetic ratio of protons. The application of oscillating magnetic field gradients synchronized to the mechanical vibration enables the measurement of arbitrary displacement components u_i in the bulk of a sample directly at the positions and in the vicinity of the scattering entities. This technique, known as magnetic resonance elastography (MRE), has successfully been employed for imaging the elastic properties of *in vivo* soft tissues [15–17]. MRE is a relatively slow technique with image acquisition times on the order of seconds, while typical shear wave speeds studied in MRE are on the order of a few meters per second.

^(a)E-mail: sebastian.papazoglou@charite.de

The onset of external vibrations relative to the begin of motion encoding determines the phase at which the local oscillations are measured. For time resolution an MRE experiment therefore requires a series of image acquisitions at different oscillation phases. Our study of Anderson localization of shear waves is based on an analysis of intensity $I = |u|^2$ of harmonic shear waves.

Intensity distribution in a multiple scattering medium. – According to the scaling theory of localization, all solutions of the stationary wave equation are localized in two or fewer dimensions [18]. However, the localization length ξ in two-dimensional systems may be exponentially large, rendering the observation of localization difficult in weakly scattering samples of size $L \ll \xi$ [19]. This obstacle is less of a problem in strongly scattering samples at low densities, when scattering is independent [20]. A measure for the scattering strength, or disorder strength, is given by the product of the wave number and the mean free path kl . The regime in which Anderson localization should be observable may then be characterized by a set of four length scales: wavelength $\lambda = 2\pi/k$, mean free path l , sample size L and dissipative absorption length l_a . In terms of these length scales the regime of localization can be expressed by the inequality $\lambda \sim l \ll L < l_a$. The first “equality” is the well-known Ioffe-Regel criterion [21]. The first inequality ensures that multiple scattering occurs inside the sample and the last inequality has to be satisfied in order to exclude dissipation as a confounder of localization. The mean free path in the Ioffe-Regel criterion is given in the literature either by $l = l_e$ with l_e the elastic mean free path or by $l = l_B$ with l_B being the Boltzmann mean free path, *i.e.* the unrenormalized transport mean free path (*e.g.* [11,22]). We will give estimates for both cases that will help to classify the regime of our experiments. For analyzing our intensity data we use the distribution of transmitted intensities determined via perturbation theory [23]. In case of an incident plane wave, the probability density of the normalized intensity $\hat{I} \equiv I/\langle I \rangle$ (where the angles denote the spatial mean) is given by

$$p(\hat{I}) = \int_0^\infty \frac{dv}{v} \int_{-i\infty}^{i\infty} \frac{ds}{2\pi i} \exp\left[-\frac{\hat{I}}{v} + sv + \Psi(s)\right], \quad (1)$$

where $\Psi(s) = g \ln^2(\sqrt{1+s/g} + \sqrt{s/g})$ and g is the dimensionless conductance. If transport of wave energy is diffusive throughout the sample, $p(\hat{I})$ is expected to be an exponential distribution $p(\hat{I}) \sim \exp(-\hat{I})$ [5]. A deviation from this kind of statistics at large intensities towards a rather stretched exponential, *i.e.* $p \sim \exp(-2\sqrt{g\hat{I}})$ indicates that diffusion has slowed down. In case of a localized state, the dimensionless conductance is expected to behave as

$$g \approx \exp(-2L/\xi(L)), \quad (2)$$

which can be employed to estimate the localization length on basis of g . A value $g < 1$ (Thouless’ criterion [24])

is combined with the Ioffe-Regel criterion for deciding whether Anderson localization has occurred. The probability $P(\hat{I})$ of finding a certain value $\hat{I} \in [\hat{I} - \Delta\hat{I}/2, \hat{I} + \Delta\hat{I}/2]$ is obtained by integrating $p(\hat{I})$ given by eq. (1) over the interval $\Delta\hat{I}$.

Multifractality. – Recent theoretical and experimental studies have focused on the multifractality (MF) of the wave intensity distribution at the transition to localization, *i.e.* at criticality [25–27]. There, the normalized intensity was shown to obey a scaling law $\hat{I}(\mathbf{r}) \propto L^{-\alpha}(\mathbf{r})$, with a continuum of possible values for α . The set of all positions \mathbf{r} at which $\hat{I}(\mathbf{r})$ scales with α can be assigned a fractal dimension $f(\alpha)$, which is called the singularity spectrum. By dividing the disordered system into equally sized square boxes B_j of length b , the scaling can quantitatively be assessed through the q -th moment of the inverse participation ratios P_q called the generalized inverse participation ratios (GIPR)

$$P_q = \sum_{j=1}^N (\hat{I}_{B_j})^q = \sum_{j=1}^N \left[\int_{B_j} \hat{I}(\mathbf{r}) d^2\mathbf{r} \right]^q. \quad (3)$$

At the localization transition the ensemble averaged GIPR scale with the dimensionless length b/L as

$$\langle P_q \rangle \sim (b/L)^{\tau(q)} = (b/L)^{d(q-1) + \Delta_q}, \quad (4)$$

where d is the Euclidean dimension and Δ_q is the anomalous scaling exponent associated with the q -th moment, that occurs at criticality. In contrast, $\Delta_q = 0$ for all values q suggests perfectly extended states. From the exponents $\tau(q)$ the singularity spectrum $f(\alpha)$ can be deduced by means of a Legendre transformation

$$\alpha = \frac{d\tau(q)}{dq}, \quad q = f'(\alpha), \quad (5)$$

$$f(\alpha) = \alpha q - \tau(q).$$

Both Δ_q and $f(\alpha)$ are convex functions and are expected to be parabolic close to their maximum, which is located at $q_0 = 1/2$ for Δ_q and at $\alpha_0 \geq d$ for $f(\alpha)$ with $f(\alpha_0) = d$. For strong disorder and increasingly large values $|q|$, the exponents Δ_q approach linearity.

Experiments and numerical simulations. – Our experimental setup was adopted from MRE using a 1.5 T MRI scanner (Sonata, Siemens, Erlangen, Germany) and a modified echo planar imaging (EPI) sequence [28]. Motion sensitization was achieved by oscillating gradients oriented perpendicular to the image plane. We fabricated three phantoms of agarose-based Wirogel (Bego Inc., Bremen, Germany) water suspension with a ratio of 1: 5 mass partitions. Each phantom comprised one hundred parallel glass rods (Length = 120 mm, $R = 1.5$ mm) at random transverse positions fixed by parallel plates at the ends of the rods, which corresponded to fixed boundary conditions at plates and bottom of the container. Assuming a shear elasticity on the order of 10^6 kPa for the glass rods at a mass

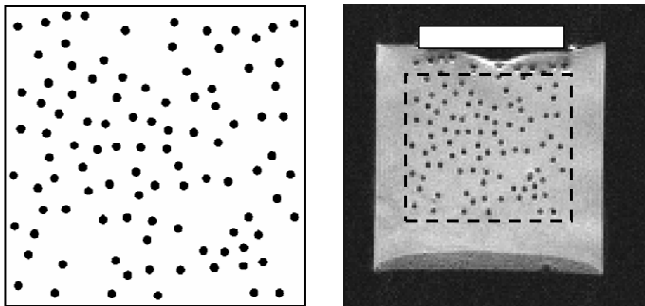


Fig. 1: The left image shows one of the templates used for positioning the glass rods inside the gel phantom. An MR magnitude image of the plane of shear wave propagation is shown on the right. The distortion on top of the phantom is an artifact due to accumulated water squeezed out of the gel by the load of the actuator plate (symbolically shown as a white bar). The dashed line demarcates the region employed in the analysis of shear wave intensities.

density of 2500 kg/m^3 , the phase speed ratio glass/gel is on the order of 10^3 . To our knowledge this is the largest ratio studied experimentally in classical multiple-wave scattering so far. Three distinct disorder configurations were determined inside a 10 cm square region using a random numbers generator (normally distributed) of Matlab (The MathWorks Inc. Natick, MA) and used as templates for positioning the glass rods. The minimum distance between neighboring rods was $0.1 R$. The resulting scatterer density was 7.1% and consequently the average distance between the rods was 0.01 m. We used a square vibrator plate for wave excitation driven by 25, 50, 75, 100, 125, 150 and 175 Hz time-harmonic oscillations. The displacement was predominantly parallel to the rods and to the direction of the motion encoding gradient, which represents a shear horizontal (SH) wave scenario [29] not susceptible to mode conversions. Sixteen phases of a wave cycle were captured at each vibration frequency. After phase unwrapping data were temporally Fourier transformed and the complex wave image $u(\mathbf{r}, \omega)$ at vibration frequency was further used for calculating intensity speckle patterns $I(\mathbf{r}, \omega)$. On one of the phantoms we conducted an experiment at 100 Hz vibration frequency in which we successively reduced the number of rods by removing random glass rods. We measured shear waves at 80, 50, 20 rods and finally without rods, corresponding to rod densities of 5.7%, 3.5%, 1.4% and zero percent, respectively. At each density we acquired data at six frequencies between 95 Hz and 105 Hz, to reduce statistical fluctuations. In our analysis we focussed on the region of interest (ROI) corresponding to the location of the scatterers as shown for one disorder configuration in fig. 1. The size of the ROI was approximately $9.5 \times 10 \text{ cm}$ corresponding to 63×70 pixels at a resolution of 1.5 mm per pixel. Two strips of width $\lambda/2$ on the left and on the right of the region of interest were excluded to suppress biases due to wave intensity leaking into the array of rods

Table 1: Ioffe-Regel parameter kl_e in the frequency range of the experiments according to first-order and second-order calculations (in the scatterer density) and simulations.

f (Hz)	25	50	75	100	125	150	175
ISA	1	1.7	2.5	3.4	4.4	5.3	6.3
2. Order + hole corr.	0.9	1.6	2.2	2.8	3.5	4.3	5.2
Simulations	0.2	0.4	1.2	1.8	2.9	3.7	4.7

from the sides. As a consequence, the number of pixels at which the intensity was evaluated ranged between 770 and 4270, depending on the vibration frequency. The normalized intensities were binned into 30 equally sized intervals between their corresponding minimum and maximum values. The resulting histograms were normalized in order to represent probabilities. Employing the bins as integration intervals $\Delta \hat{I}$, we fitted $P(\hat{I})$ to the histograms by varying g between 0.02 and 10. This procedure was applied to every frequency and disorder configuration individually. Finally, the determined values for the dimensionless conductance were averaged. In order to estimate the Ioffe-Regel parameter in our experiments, we spatially Fourier-transformed wave data averaged over the six frequencies around 100 Hz and applied a directional filter with maximum amplitude in downwards direction [29]. The decay in the back-transformed wave image was then fitted to determine the elastic mean free path l_e as described in the results section. This procedure was repeated for each rod density. We also determined the GIPR from the experiments with different numbers of glass rods using box sizes $B_j = \{7, 10, 14, 35\}$ pixels and varying q between -6 and $+6.5$ in steps of 0.025. The anomalous scaling exponents Δ_q were determined from linear fits to the logarithm of eq. (4). The singularity spectrum $f(\alpha)$ was then computed according to eqs. (5) using standard numerical differentiation. For comparison, an experiment on an identical phantom but without scatterers was performed. In this phantom we determined the shear elasticity of the gel by manual evaluation of wavelengths with approximately 4 kPa at a mass density of 1000 kg/m^3 . This elasticity value together with sample dimensions, coordinates and density of scatterers as well as the drive frequencies used in the experiments were fed into numerical simulations employing a multiple scattering algorithm introduced in [30]. In our simulations no viscosity and no finite object boundaries were considered. Rigid boundary conditions were applied at the interfaces between matrix and scatterers for simulating the vast leap in shear elasticity at gel-glass interfaces in the experiments. At each frequency we simulated wave scattering in 200 distinct disorder configurations in order to gain an estimate of the coherent field.

Results and discussion. – We calculated the elastic mean free path numerically from the effective wave number k_{eff} , *i.e.* $l_e = 1/(2\text{Im}\{k_{eff}\})$, in the independent

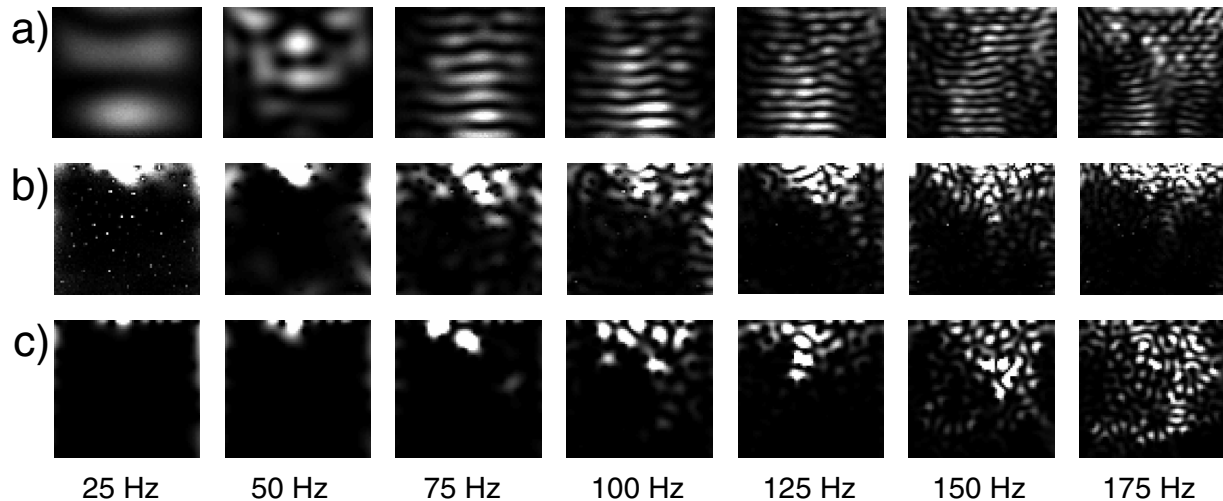


Fig. 2: Intensity normalized to its mean is shown for experiments on a) a homogeneous phantom, b) a phantom with cylindrical inclusions and c) wave scattering simulations. In both experiment and simulation, the configuration of cylindrical inclusions corresponds to fig. 1.

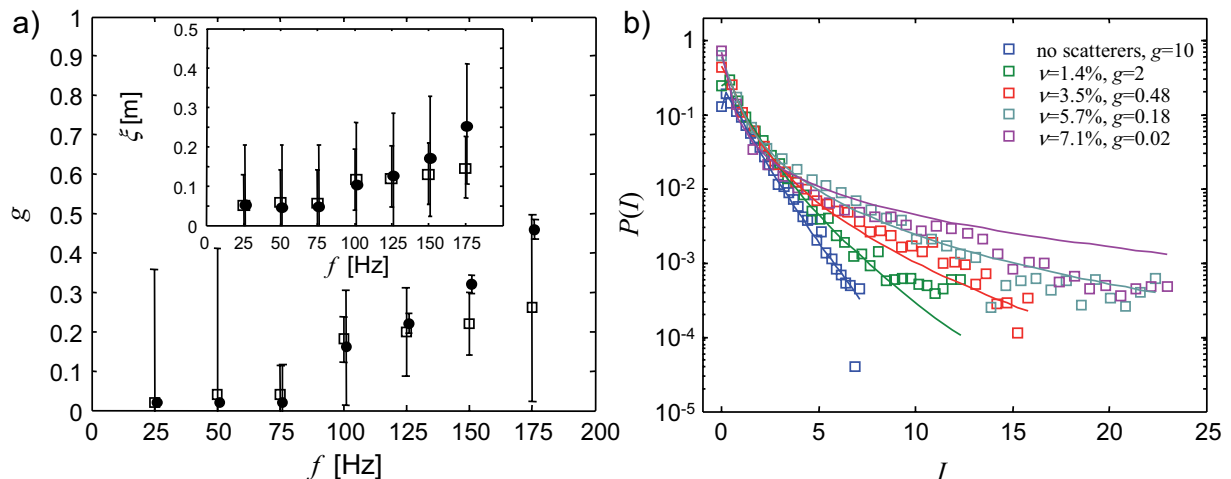


Fig. 3: a) Median of the dimensionless conductance g determined in experiments (open squares) and simulations (solid circles). The insert shows the corresponding localization length ξ determined according to eq. (2). Error bars represent 95% confidence intervals. b) Intensity distributions as a function of scatterer density determined from experimental data. Solid lines represent fits to data using eq. (1).

scatterer approximation (ISA) and using a second-order approximation combined with the so-called hole correction to account for correlations in the positions of the rods [31]. Moreover, we determined l_e from our simulations by fitting the exponential decay of the ensemble averaged fields. The results are summarized in table 1. We also calculated the Boltzmann mean free path l_B , which however, in the frequency range of our experiments deviated insignificantly from l_e . More precisely, the angle average occurring in the calculation of l_B was found to be less than 0.02 in our frequency range. In particular, no resonances were found. The results in table 1 show that both ISA and the second-order approximation overestimate the Ioffe-Regel parameter as determined from numerically simulated multiple scattering. The intensity

distribution as observed in experiments and simulations is shown in fig. 2. In case of no scatterers (fig. 2(a)), variations of the shear wave intensity are shallow and the intensity is not restricted to regions close to the source of the waves. This is in contrast to experiments and simulations with scatterers. Variations of the shear wave intensity are much more pronounced and the intensity is restricted to regions near the source of the waves. This suggests that shear wave energy is not propagated through the phantom but is accumulated in regions close to the source. Figure 3(a) shows the average dimensionless conductances determined in our experiments and numerical simulations. Considerably low values $g < 1$ are found at all frequencies, whereby experiments and simulations agree within the error margins. In contrast to [13] and [14] we cannot

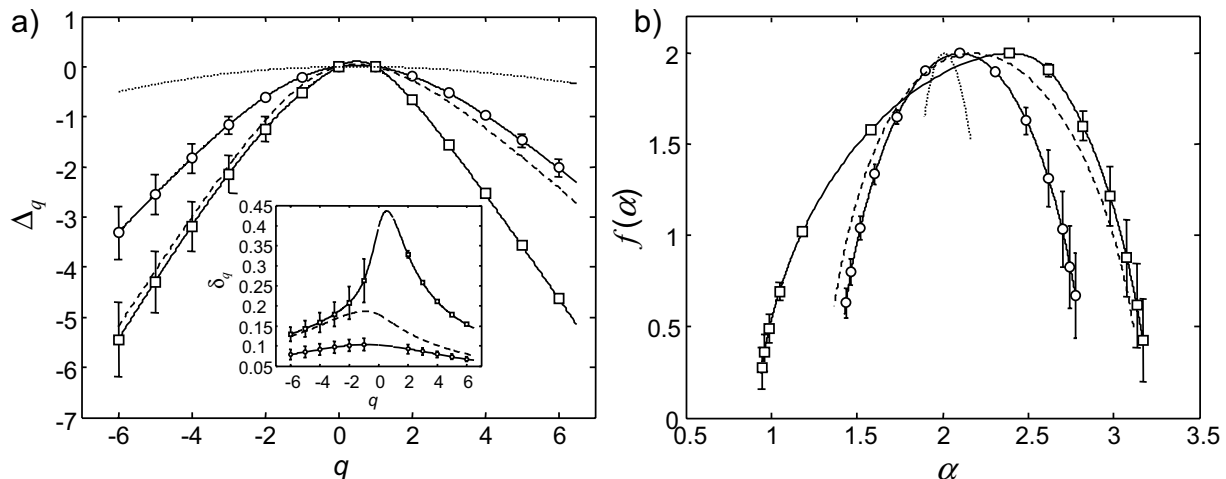


Fig. 4: a) The anomalous scaling exponents at 100 Hz and 7.1% (open squares), 3.5% (dashed line) and zero percent (open circles) scatterer density. The dotted lines represents the anomalous exponents determined from Gaussian noise. The insert shows the deviation from parabolicity. For further explanation see the discussion. b) The singularity spectrum corresponds to the data in a). Error bars represent 95% confidence intervals.

measure the localization length directly due to overlapping intensity peaks. Furthermore, the harmonic steady state does not allow an analysis of the dynamics of localization. From the dimensionless conductance we can nevertheless estimate the localization length $\xi(L)$ according to eq. (2), which is shown in the insert of fig. 3(a). A low value g represents a strong deviation from Rayleigh statistics, which in combination with the expected values for the Ioffe-Regel parameter (table 1) suggests that shear waves are localized. This conclusion is further supported by fig. 3(b). There it is shown that decreasing the number of glass rods yields monotonically increasing g , with a threshold for $g < 1$ between $\nu = 3.5\%$ and 1.4% . In case of no glass rods, an exponential distribution is observed as is expected for purely diffusive transport or pure Gaussian noise. However, it is important to note that eq. (1) was derived for the 2d distribution of transmitted intensity in case of a 3d slab geometry, while our observations are based on 2d intensities inside a 3d geometry. This issue requires further theoretical investigation as does the fact that eq. (1) was derived on basis of a mean-field approximation, which is not expected to completely describe the features of strong localization. The Ioffe-Regel parameter at 100 Hz was found with $kl_e = 2.6, 5.8, 9.4, 12.5$ and 28.2 at scatterer densities of 7.1%, 5.7%, 3.5%, 1.4% and 0%, respectively. Compared to table 1 the value $kl_e = 2.6$ at 7.1% density is somewhat larger than predicted by our simulations, which is likely due to the directional filtering yielding only estimates of the coherent field required for determining l_e . To analyze dissipation, we determined the spatially averaged l_a from the experiment on the phantom without scatterers by using an inverse algorithm similar to [28]. We found values $l_a \approx 2L$ at 75 Hz and 100 Hz, suggesting no significant impact of dissipation on the observation of Anderson localized shear waves

at these frequencies. Figure 4(a) shows the anomalous scaling exponents Δ_q . There, the expected MF of critical waves is clearly visible. As predicted by analytical and numerical investigations the graphs are symmetric about $q = 1/2$. However, while the graphs at 7.1% and 0% rod density show good symmetry, data at 3.5% clearly shows an asymmetry. This is likely due to limited system size and limited number of disorder configurations. The insert shows $\delta_q = \Delta_q/[q(1-q)]$, which quantifies the deviation from a parabola, *i.e.* a constant value δ_q indicates perfect parabolicity. It is seen that the shape of Δ_q is closest to a parabola when no rods are present. Combined with the observation of Rayleigh statistics (see fig. 3(b)) and a large value of the Ioffe-Regel parameter, this suggests that wave transport is diffusive in this case. In fig. 4(b) the singularity spectrum $f(\alpha)$ is seen to be least symmetric at largest scatterer density. This again may be attributed to the small size of the system. In general, it was shown that the symmetry of the spectrum improves with increasing system size [26]. When considering the symmetry one should also notice that data Δ_q and $f(\alpha)$ are more susceptible to numerical errors at the boundaries. The positions of the maxima at values $\alpha_0 > 2$ and the value $f(\alpha_0) = 2$ are in agreement with the theory. Figure 4(b) also shows that the width increases with increasing rod density (in the range of our densities), which is also expected.

Conclusions. – In our interpretation of the results Anderson localization of shear waves has occurred due to multiple scattering of shear horizontal waves by glass rods embedded in a soft gel matrix. We used MRI in combination with an experimental setup for generating and observing SH waves at the sites of cylindrical scatterers. Rather than measuring transmission properties, this method enables for the first time the analysis of the

distribution of shear wave intensity directly in the scattering regions of the sample. However, a precise determination of g and $\xi(L)$, respectively, would require a large number of disorder configurations or larger system sizes with a larger number of glass rods. This is reflected by the large fluctuations in g seen in the errors in fig. 3(a) and by the degree of symmetry of Δ_q and $f(\alpha)$. Similar to [14] we nevertheless consider it as an estimator for the deviation from Rayleigh statistics. As demonstrated in fig. 3(b), the diffusive regime is well observable with our method. Without glass rods scattering still occurs, although much less effective, from the remaining water-filled holes in the gel matrix, which is also well reflected by the anomalous scaling exponents and the singularity spectrum in figs. 4(a) and (b), respectively. The good agreement with our 2d simulations (where no dissipation was included) further supports that we observed strongly localized shear waves in the frequency range around 100 Hz. A clearly observable MF spectrum underlines the criticality of the wave function at this frequency and a rod density of 7.1%. Aside from being an interesting new modality for studying Anderson localization of shear waves in particular and multiple scattering of shear waves in heterogeneous soft materials in general, the employed MRI method is uniquely suited to analyze shear wave scattering inside the human body independently of acoustic ultrasound windows.

REFERENCES

- [1] FOLDY L. L., *Phys. Rev.*, **67** (1945) 107.
- [2] LETOKHOV V., *Sov. Phys. JETP*, **26** (1968) 835.
- [3] BERGMANN G., *Phys. Rev. B*, **28** (1983) 2914.
- [4] ANDERSON P. W., *Phys. Rev.*, **109** (1958) 1492.
- [5] SHENG P., *Introduction to Wave Scattering, Localization and Mesoscopic Phenomena* (Springer-Verlag, Berlin, Heidelberg) 2006.
- [6] MOTT N. F., *Rev. Mod. Phys.*, **40** (1968) 677.
- [7] ALBADA M. P. V. and LAGENDIJK A., *Phys. Rev. Lett.*, **55** (1985) 2692.
- [8] WEAVER R., *Wave Motion*, **12** (1990) 129.
- [9] GENACK A. Z. and GARCIA N., *Phys. Rev. Lett.*, **66** (1991) 2064.
- [10] WIERSMA D., BARTOLINI P., LAGENDIJK A. and RIGHINI R., *Nature*, **390** (1997) 671.
- [11] STOERZER M., GROSS P., AEGERTER C. and MARET G., *Phys. Rev. Lett.*, **96** (2006) 063904.
- [12] SCHWARTZ T., BARTAL G., FISHMAN S. and SEGEV M., *Nature*, **446** (2007) 52.
- [13] LAURENT D., LEGRAND O., SEBBAH P., VANNESTE C. and MORTESSAGNE F., *Phys. Rev. Lett.*, **99** (2007) 253902.
- [14] HU H., STRYBULEVYCH A., PAGE J. H., SKIPETROV S. E. and VAN TIGGELEN B. A., *Nat. Phys.*, **4** (2008) 945.
- [15] MUTHUPILLAI R., ROSSMAN P., LOMAS D., GREENLEAF J., RIEDERER S. and EHMAN R., *Magn. Reson. Med.*, **36** (1996) 266.
- [16] VAN HOUTEN E., DOYLEY M., KENNEDY F., WEAVER J. and PAULSEN K., *J. Magn. Reson. Imaging*, **17** (2003) 72.
- [17] SACK I., BEIERBACH B., WUERFEL J., KLATT D., HAMHABER U., PAPAZOGLU S., MARTUS P. and BRAUN J., *Neuroimage*, **46** (2009) 652.
- [18] ABRAHAMS E., ANDERSON P. W., LICCIARDELLO D. C. and RAMAKRISHNAN T. V., *Phys. Rev. Lett.*, **42** (1979) 673.
- [19] LEE P. A. and RAMAKRISHNAN T. V., *Rev. Mod. Phys.*, **57** (1985) 287.
- [20] VAN TIGGELEN B., LAGENDIJK A., TIP A. and REITER G., *Europhys. Lett.*, **15** (1991) 535.
- [21] IOFFE A. and REGEL A., *Prog. Semicond.*, **4** (1960) 237.
- [22] GÓMEZ RIVAS J., SPRIK R., LAGENDIJK A., NOORDAM L. D. and RELLA C. W., *Phys. Rev. E*, **62** (2000) R4540.
- [23] NIEUWENHUIZEN T. M. and VAN ROSSUM M. C. W., *Phys. Rev. Lett.*, **74** (1995) 2674.
- [24] THOULESS D., *Phys. Rep.*, **13** (1974) 93.
- [25] EVERS F. and MIRLIN A. D., *Rev. Mod. Phys.*, **80** (2008) 1355.
- [26] VASQUEZ L. J., RODRIGUEZ A. and RÖMER R. A., *Phys. Rev. B*, **78** (2008) 195106.
- [27] FAEZ S., STRYBULEVYCH A., PAGE J. H., LAGENDIJK A. and VAN TIGGELEN B. A., *Phys. Rev. Lett.*, **103** (2009) 155703.
- [28] KLATT D., HAMHABER U., ASBACH P., BRAUN J. and SACK I., *Phys. Med. Biol.*, **52** (2007) 7281.
- [29] PAPAZOGLU S., HAMHABER U., BRAUN J. and SACK I., *Phys. Med. Biol.*, **52** (2007) 675.
- [30] BIWA S., YAMAMOTO S., KOBAYASHI F. and OHNO N., *Int. J. Solids Struct.*, **41** (2004) 435.
- [31] DERODE A., MAMOU V. and TOURIN A., *Phys. Rev. E*, **74** (2006) 036606.